Dynamics of nevus development implicate cell cooperation in the growth arrest of transformed melanocytes

Rolando Ruiz-Vega[1,2], Chi-Fen Chen[3], Emaad Razzak[1], Priya Vasudeva[3], Tatiana B. Krasieva[4], Jessica Shiu[3], Michael G. Caldwell[1], Huaming Yan[5], John Lowengrub[1,5], Anand Ganesan[1,3,6], Arthur D. Lander[*1,2]

1. Center for Complex Biological Systems, University of California Irvine, Irvine CA, 92697, USA.
2. Department of Developmental and Cell Biology, University of California Irvine, Irvine CA, 92697, USA.
3. Department of Dermatology, University of California Irvine, Irvine CA, 92697, USA.
4. Beckman Laser Institute, University of California Irvine, Irvine CA, 92697, USA.
5. Department of Mathematics, University of California Irvine, Irvine CA, 92697, USA.
6. Department of Biological Chemistry, University of California Irvine, Irvine CA, 92697, USA.
*Correspondence: adlander@uci.edu

Keywords:

Nevi, melanocytes, Braf mutation, oncogene induced senescence, nevus mouse model, skin, nevus growth arrest, systems biology, clonal dynamics, pigment, live mouse imaging, SASP, senescence

Short Title: Cooperative dynamics in melanocyte growth arrest

1 **Abstract**

2 Mutational activation of the BRAF proto-oncogene in melanocytes reliably produces benign nevi

3 (pigmented "moles"), yet the same change is the most common driver mutation in melanoma. The

4 reason nevi stop growing, and do not progress to melanoma, is widely attributed to a cell-

5 autonomous process of "oncogene-induced senescence". Using a mouse model of Braf-driven

6 nevus formation, analyzing both proliferative dynamics and single-cell gene expression, we found

7 no evidence that nevus cells are senescent, either compared with other skin cells, or other

8 melanocytes. We also found that nevus size distributions could not be fit by any simple cell-

9 autonomous model of growth arrest, yet were easily fit by models based on collective cell

10 behavior, e.g. in which arresting cells release an arrest-promoting factor. We suggest that nevus

11 growth arrest is more likely related to the cell interactions that mediate size control in normal

12 tissues, than to any cell-autonomous, "oncogene-induced" program of senescence.

13

14 **INTRODUCTION**

15 Activating BRAF mutations (e.g. BRAF^{V600E}) are the most common oncogenic mutations in

16 melanoma, seen in about 66% of cases (Davies et al., 2002). Curiously, the same mutation is

17 found in 89% of melanocytic nevi (Pollock et al., 2003)—the benign, pigmented "moles" found on

18 the skin of most individuals. In animal studies, melanocyte-specific expression of BRAF^{V600E}

19 efficiently produces nevi, but only very rarely melanoma (Dankort et al., 2009; Dhomen et al.,

20 2009; Patton et al., 2005). The widely-accepted explanation is that transformed melanocytes

21 undergo oncogene-induced senescence (OIS), arresting proliferation before additional oncogenic

22 events can occur (e.g. Bennett, 2003; Huang et al., 2017; Kaplon et al., 2014; Michaloglou et al.,

23 2005).

24 Nevus melanocytes are indeed growth-arrested, but the assumption that OIS is the cause

25 remains untested, in part because of a lack of criteria to rigorously define OIS in vivo (Damsky &

26 Bosenberg, 2017). Initially studied as a consequence of forced expression of oncogenes in cell

27 cultures (Serrano et al., 1997), OIS has come to be seen as a distinctive cellular stress response

28 characterized by a phenotype of growth arrest, morphological and metabolic changes, chromatin

29 alterations, and secretion of growth factors, chemokines, cytokines and proteases (Campisi &

30 d'Adda di Fagagna, 2007; Gorgoulis et al., 2019; Ito et al., 2017; Kuilman et al., 2010).

31 Given an abundance of "hallmarks" of senescence, one might think that recognizing this cell

32 state in vivo should be straightforward. Yet no single hallmark distinguishes senescence from

33 other growth-arrested cell states. Phenotypes once thought to be "gold standards", such as

34   expression of lysosomal beta-galactosidase, cyclin-dependent kinase inhibitors, or p53,

35   commonly mark only subsets of senescent cells (Wiley et al., 2017), as well as non-senescent

36   cells (Tran et al., 2012).   Moreover, observations of supposedly senescent cells resuming

37   proliferation (e.g. Beausejour et al., 2003), imply that permanent cell cycle exit cannot be used as

38   a distinguishing feature. In vivo senescence, as a result, is currently somewhat of a *Gestalt*

39   diagnosis, i.e. assessed by a collection of traits, no subset of which is necessary or sufficient. Yet

40   there is no clear consensus on which traits are best to assess, and recent meta-analyses of gene

41   expression suggest that some of the most commonly assessed features are not "core" to

42   senescence at all (Hernandez-Segura et al., 2017).

43   The reason it is important to clarify how BRAF-transformed nevus melanocytes stop growing

44   is that it shapes how we think about the origins of melanoma. OIS is usually portrayed in *cell-*

45   *intrinsic* terms: oncogene expression within a transformed cell produces a stress within *that* cell,

46   which triggers *it* to senesce. Even those who acknowledge a possible role for paracrine signals

47   (Acosta et al., 2013; Elzi et al., 2012; Ito et al., 2017; Wajapeyee et al., 2008) still portray the

48   process as something initiated and orchestrated by cell-autonomous responses to oncogenes.

49   This naturally leads to an approach to melanoma prevention and treatment that focuses on

50   understanding how oncogenes derange intracellular processes; how those derangements elicit

51   stress responses; and what might enable cancer cells to circumvent those responses (e.g.

52   Bennett, 2003; Damsky & Bosenberg, 2017; Vredeveld et al., 2012; Yu et al., 2018). In contrast,

53   as we argue below, it is possible that the growth arrest displayed by nevus melanocytes has little

54   to do with oncogene-induced stress, and may have more to do with networks of cell-cell

55   communication that are characteristic of melanocytes, independent of whether they are

56   transformed. In this case, the most effective path to understanding how to prevent or treat

57   melanoma could be to better elucidate the normal physiology of melanocytes in their environment.

58   Here, we investigate the details of nevus growth arrest in a model in which melanocyte-

59   specific *Braf* activation generates hundreds of nevi on the skin of mice (Dankort et al., 2009). By

60   examining both single-cell transcriptomes and the dynamics of growth arrest in nevus-associated

61   melanocytes, we make two key observations: First, patterns of gene expression in arrested nevus

62   melanocytes fail to identify them as any more senescent than other skin cells or normal

63   melanocytes, arguing against a primary role for any form of senescence in their arrest. Second,

64   the timing and statistics of nevus formation effectively argue against *any* relatively simple cell-

65   autonomous process as being the cause of growth arrest. Ultimately, we propose a model in

66   which arrest is driven not by oncogene stress, but by feedback mechanisms similar to those

67 commonly involved in normal tissue homeostasis.

68 **RESULTS**

69 **Dynamics of nevus growth**

70 Characterizing the dynamics of nevus growth and arrest requires observing nevi that started

71 growing at known times. We took advantage of a mouse model in which Cre-mediated

72 recombination introduces the activating V600E mutation into the endogenous *Braf* locus. When

73 crossed onto a background carrying a *Tyr::CreER* transgene, the mice acquire the *Braf*^{V600E}

74 mutation only in cells of the melanocytic lineage, and only after Cre activation by 4-

75 hydroxytamoxifen (4-OHT), applied either systemically or through painting on the skin.

76 As shown previously (Dankort et al., 2009), 4-OHT treatment of these mice leads to

77 development of numerous pigmented nevi. Visualization of nevi is hindered, however, by the

78 strong pigmentation in hair follicles which, except at microscopic resolution, can be difficult to

79 distinguish from nevi. One way to circumvent this difficulty is to observe nevi only during the

80 telogen phase of the hair cycle, when follicle-associated pigment is not present (conveniently,

81 synchronization of hair cycles may be maintained on a large patch of skin through depilation).

82 As shown in Figure 1, in mice whose back skin was treated with topical 4-OHT at postnatal

83 day 2 (P2), P3 and P4, nevi were apparent macroscopically at telogen (P50; Fig. 1A). Live-

84 imaging, using multi-photon microscopy (MPM; (Saager et al., 2015)), revealed that, like human

85 nevi, mouse nevi consist of scattered nests of pigment-containing cells (Fig. 1B). Nevi could also

86 be visualized post-mortem, using a dissecting microscope, on the undersurface of pieces of

87 telogen-stage back skin (Fig. 1C).

88 An alternate approach to visualization that did not require hair synchronization was to

89 generate nevi by painting 4-OHT on glabrous (hairless) skin, such as the ventral surface of the

90 paw, permitting tracking of individual nevi on a daily basis. As shown in Fig. 1D, when forepaws

91 were treated with 4-OHT from P2 through P4, tiny nevi could be detected as early as P6. Serial

92 observation indicated that most nevi reach a maximum size somewhere between P16 and P21

93 (Fig. 1D and S1A). This suggests that, in the mouse, *Braf*^{V600E} -transformed melanocytes arrest

94 within 2-3 weeks. To confirm this, we used BrdU labeling to monitor DNA synthesis. Because

95 melanin readily obscures immunohistochemical signals, these experiments were done in an

96 albino (unpigmented) genetic background, using premelanosome protein (Pmel) staining to

4
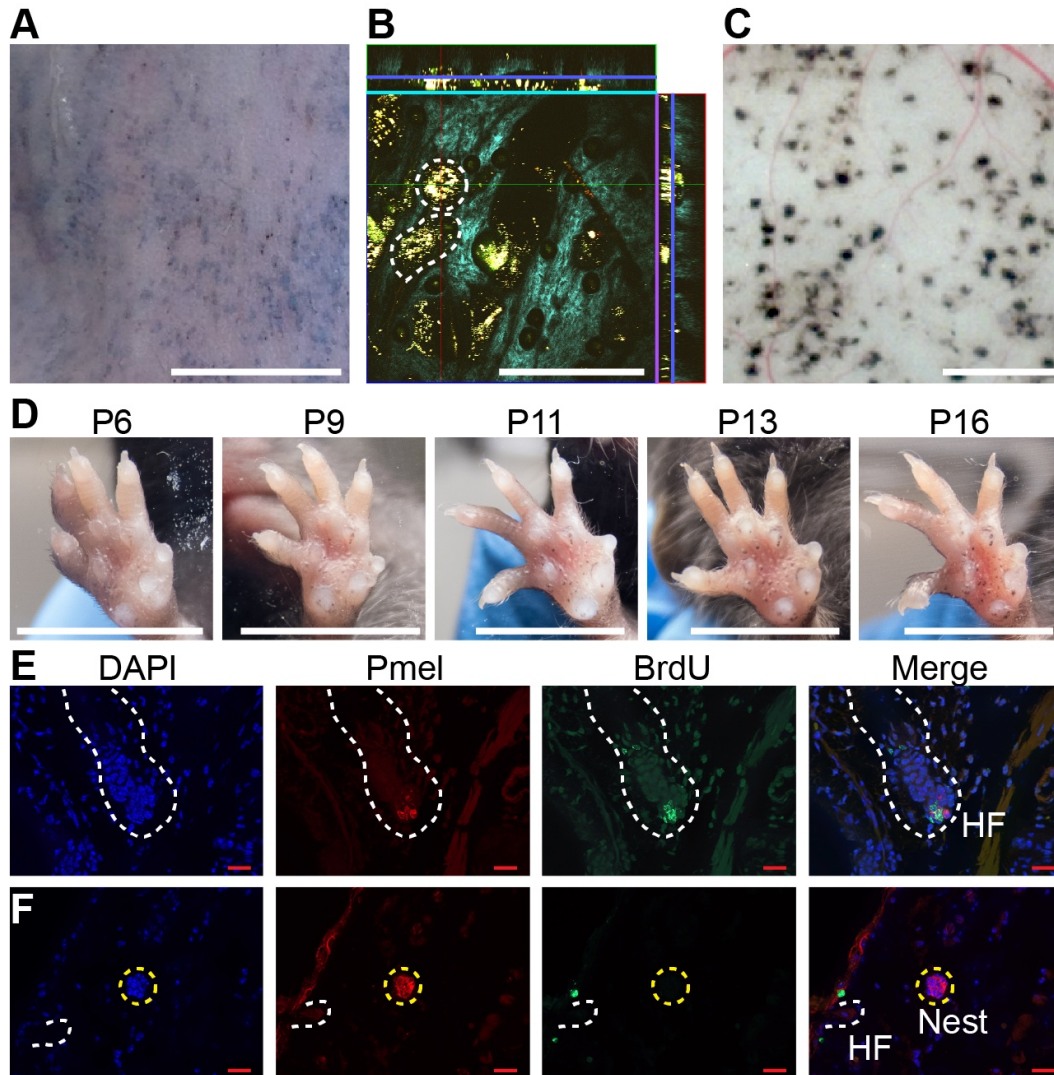
97

Figure 1. Dynamics of nevus growth. **A-D.** Visualization of nevi on Braf[V600E] mice. (A) Live imaging of back skin at telogen stage (P50), following hair depilation. Scale bar = 5 mm. (B) Live imaging of a sample like that in panel A using multiphoton microscopy. The central square is an *en face* view of the skin (*x-y* plane), while rectangles above and to the right are cross-sections (*x-z* and *y-z* planes, respectively, with blue lines marking the location of the central image). Melanin autofluorescence appears yellow, second harmonic generation of collagen is cyan, and keratin autofluorescence is green. Dashing outlines dermal melanocyte nests. Scale bar = 318 µm. (C) Appearance of nevi on the undersurface of back skin (at P21). Scale bar = 1 mm. (D) Nevus development on the ventral (glabrous) surface of the paw. Images of a single paw were taken at the indicated ages. Scale bar = 0.5 cm. **F.** Assessment of melanocyte proliferation. Sections are from albino wildtype (E) and Braf[V600E] (F) skin at P21. Melanocytes were identified by premelanosome protein (Pmel) immunohistochemistry and proliferation assessed by BrdU incorporation. Wildtype hair follicle (HF) melanocytes (E) incorporate BrdU whereas nevus melanocytes (F) do not. Scale bar = 20µm.

5

98 identify melanocytes. As shown in Fig. 1F, albino mice generate nests similar to those seen in

99 pigmented mice. In such animals, BrdU readily incorporated into hair follicle melanocytes (Fig.

100 1E, S1B), whereas by p21 nests within nevi were uniformly negative for BrdU, implying growth

101 arrest (Fig. 1F, S1C).

102 The conclusion that Braf-induced nevi are already growth-arrested by P21 agrees with the

103 reports of others (Damsky & Bosenberg, 2017), and is lent further support by time course

104 measurements of nest size by MPM (Fig. 1C), which show that nest size distributions change

105 insignificantly between P21 and P50 (Fig. S4A-B).

106

107 **Do nevi undergo "oncogene-induced senescence"?**

108 As discussed above, senescence is usually accompanied by distinctive gene expression.

109 Various gene expression "signatures" have been developed to help investigators identify

110 senescent cells and distinguish them from cells that have become growth arrested by other

111 processes. We considered several of these (Data S1):

112 1) A set of genes encoding the most commonly considered "hallmarks" of senescence, i.e.

113 p53, Rb, lysosomal beta-galactosidase, H2AX, and three cyclin-dependent-kinase inhibitors

114 ("Classical", 7 genes (Campisi & d'Adda di Fagagna, 2007; Collado & Serrano, 2006));

115 2) A gene signature that distinguishes cultured human fibroblasts growth arrested by BRAF-

116 transformation from quiescent fibroblasts ("Kuilman", 21 genes (Kuilman et al., 2008))

117 3) Results of a meta-analysis (Hernandez-Segura et al., 2017)) of publications on fibroblasts,

118 melanocytes, and astrocytes, comparing senescence (induced by multiple different stresses) with

119 quiescence, yielding "universal" signatures of genes that are up- and down-regulated specifically

120 in senescence ("Universal Up", 31 genes, and "Universal Down", 23 genes) as well as signatures

121 of genes specifically up- or down-regulated by senescence induced in melanocytes ("Melanocyte

122 Up", 397 genes and "Melanocyte Down", 135 genes).

123 4); The most statistically significant genes in a recent meta-analysis (Chatsirisupachai et al.,

124 2019) of 20 replicative senescence microarray datasets from the Gene Expression Omnibus

125 ("Chatsirisupachai Up", 237 genes and "Chatsirisupachai Down", 244 genes).

126 5) A list of genes characteristic of the "Senescence-Associated Secretory Phenotype"

127 ("SASP", 81 genes), compiled from 38 literature references (for citations see Data S1).

128 To determine whether any of these proposed signatures fits nevus melanocytes, we

129 performed single cell RNA-sequencing on dissociated cells from the back skin of nevus-bearing

130   mice at both P30 and P50 (i.e. after nevi have stopped growing), using wildtype skin as a control.

131   Using known cell-type marker genes (Fig. S2A-B), we identified 14 different cell types in the skin,

132   including melanocytes (Fig. 2A). Unsupervised clustering further sub-divided the melanocytes

133   into four groups (Fig. 2B): Two of them, Mel 0 and Mel 1, were composed of cells found only in

134   nevus-bearing, and not wild-type, skin (Fig. 2C); they are highly similar in gene expression,
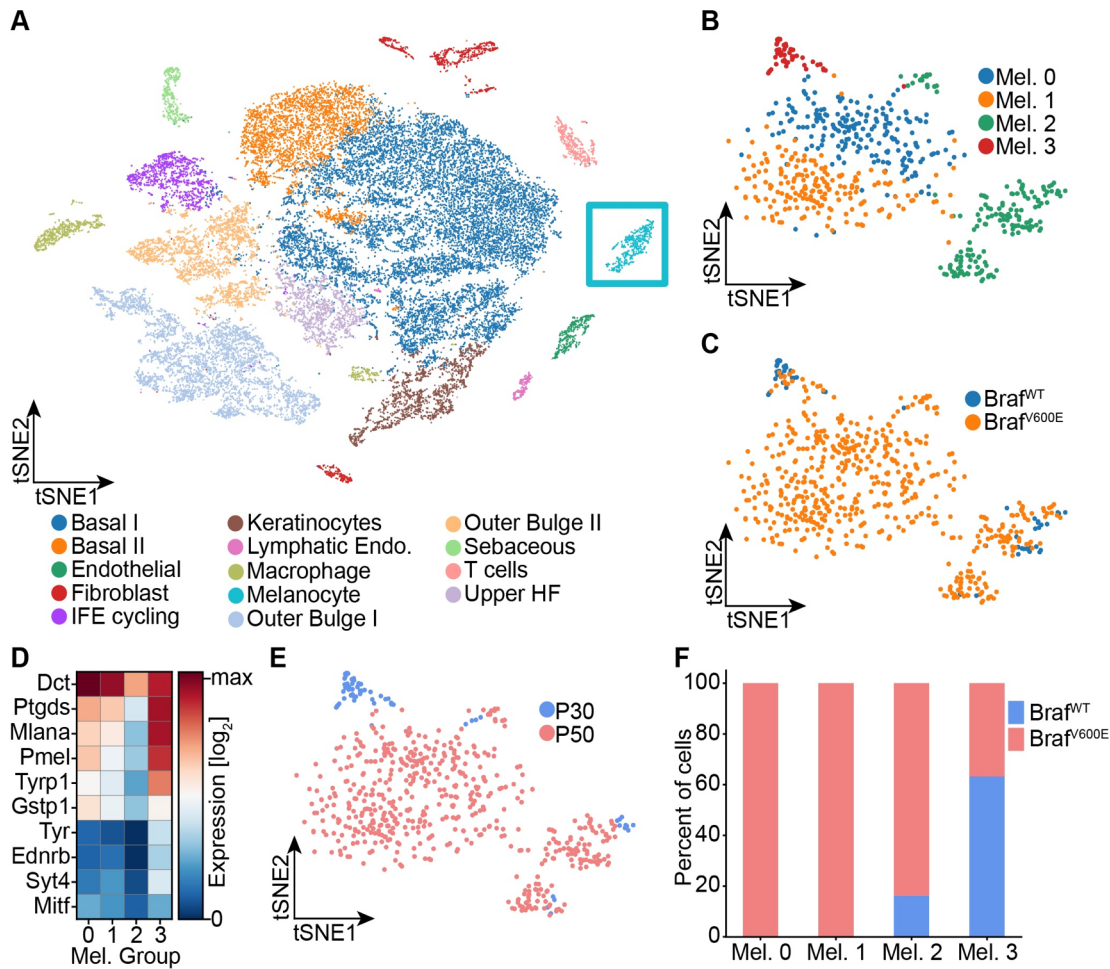
Figure 2. Single cell RNA sequencing of mouse dorsal skin to transcriptionally characterize melanocytes. **A.** Skin cell types are visualized with tSNE (cells = 35,141) from mice at P30 (n[Braf^{WT}] = 2 mice, n[Braf^{V600E}] = 2 mice) and P50 (n[Braf^{WT}] = 3 mice, n[Braf^{V600E}] = 3 mice). Melanocytes are outlined with a blue box. **B.** Subclustering of melanocytes (n = 609) and visualized on a tSNE plot. Four clusters were identified. **C.** Visualization of melanocytes based on their genotype on a tSNE plot. **D.** A heat map of different genes involved in pigmentation. Each cluster expresses these genes at different levels. **E.** Visualization of melanocytes based on their age on a tSNE plot. **F.** Quantification of melanocytes in each cluster based on their genotype BRAF wild-type or mutant mice.

7

135 primarily differing in having a slightly lower level of pigment gene expression in Mel 1 versus Mel

136 0 (Fig. 2D). We identify them as the "nevus melanocytes", because they are seen only when nevi

137 are present, and are by far the predominant melanocyte population in such animals.

138 Mel 2 cells express the lowest levels of pigmentation genes (Fig. 2D), and are seen in both

139 genotypes (Fig. 2C) at all stages (although expanded in number in nevus-bearing animals (Fig.

140 2F)). Their pattern of gene expression bears a strong resemblance to one recently published for

141 melanocyte stem cells isolated from telogen-stage hair follicles (Zhang et al., 2020). In particular,

142 they express *Cd34*, which has been proposed to be a marker for bulge-associated melanocyte

143 stem cells (Joshi et al., 2019).

144 Finally, cells of cluster Mel 3, which express the highest levels of pigment genes (Fig. 2D),

145 are found in both mutant and wildtype mice, but only at the P30 time point (Fig. 2E-F). We thus

146 identify them as mature hair follicle melanocytes, as such cells are present exclusively during

147 anagen phase of the hair cycle (P30), and disappear during telogen (P50).

148 Because gene signatures are based on the idea of up- and down-regulation of expression

149 relative to some baseline state, to test whether nevus melanocytes fit a known signature it is

150 necessary to have comparison transcriptomes. We made two types of comparisons: nevus

151 melanocytes versus every other cell type in the skin (which, with the possible exception of mature

152 keratinocytes, we would not expect to be senescent); and the four melanocyte sub-clusters (two

153 of which are nevus-associated and two of which are not) versus each other. In each case we

154 computed average expression for each gene in every cell type or cluster, together with a standard

155 error of the mean as a measure of dispersion. Expression values were then normalized to

156 average expression across all of the cells being compared (i.e. all skin cells, or all melanocytes,

157 depending on which comparison was being done) and log_2-transformed, so that positive values

158 signify upregulation (relative to the average for that gene), and negative downregulation. Gene

159 expression was then visualized using heat maps (Fig. 3A, S3, with positive values in blue and

160 negative in red). Because gene expression levels inferred from single cell RNA sequencing tend

161 to be noisy, particularly for genes with low expression, we ranked all genes by their minimum level

162 of noise (i.e. normalized standard error of the mean in the least noisy cell type), and used this

163 value ("n-SEM", which is also presented graphically as a bar to the right of each heatmap) to sort

164 gene lists, so that maps vary from most to least reliable as one goes from top to bottom.

165 Figure 3A shows the results for the "Classical" and "Universal Up" signatures (heat maps for

166 the other signatures are shown in Figure S3). Here we see no strong enrichment of blue over red

167 signals in nevus melanocytes, nor in most other cells. When compared with whole skin, using

168   the "Classical" signature, only *Cdkn2a* stands out as strongly upregulated in nevus melanocytes,

169   but it is similarly upregulated in skin fibroblasts (it also has the noisiest data among genes in the

170   signature). With the "Universal Up" signature, more genes are downregulated than upregulated

171   in nevus melanocytes. To quantify such impressions, we summed the log_2-transformed data in

172   each column in every heat map, producing the bar graphs in Figure 3B. We reasoned that

173   summation of log-transformed data would emphasize consistent trends in the data while
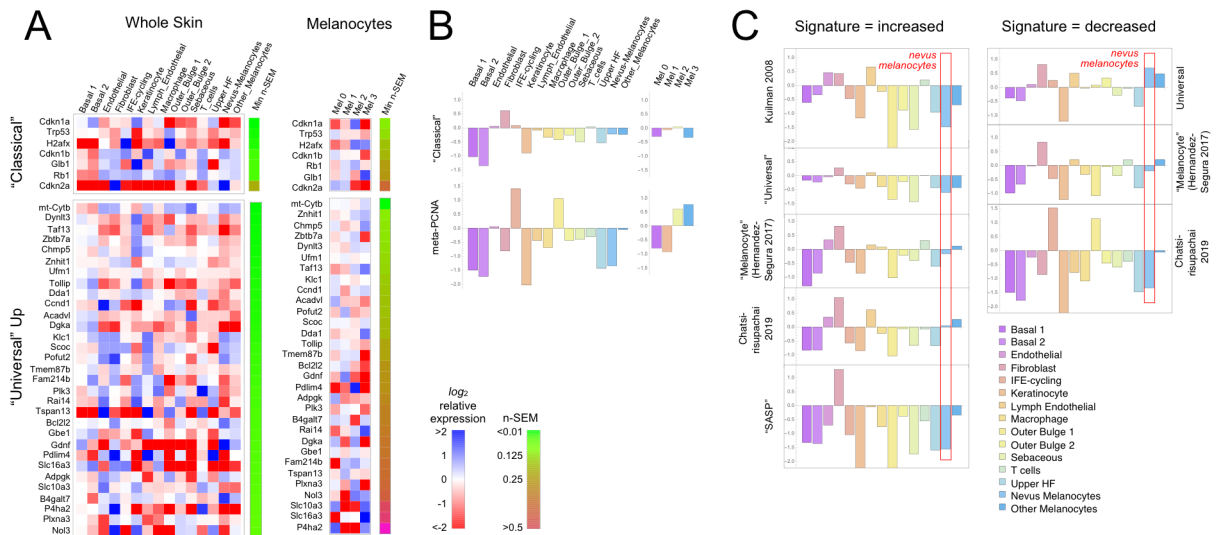
Figure 3. Gene expression fails to identify nevus melanocytes as senescent. Transcriptomes of clusters identified in Fig. 2 were compared with proposed "signatures" of senescence. **A.** Gene expression data for clusters in Fig. 2A and 2B were averaged by cluster and, for each gene, expressed as a ratio to the average expression level of that gene in the entire skin sample ("Whole Skin") or just the melanocyte clusters ("Melanocytes"). The heat map displays the logarithm of that ratio, with blue representing upregulation and red downregulation, relative to the appropriate average. Two proposed signatures for genes upregulated in senescence ("Classical" and "Universal Up") are shown (For other signatures, see Fig. S4). Gene lists have been sorted by the minimum gene expression variability within the least variable cluster (green-brown bar). **B**. The "Classical" heatmaps in panel A are summarized as a bar graph displaying the sum of the log-transformed data. Also shown are summary results for a proposed signature of proliferation, "meta-PCNA", which clearly distinguishes between cell types expected to be proliferative and non-proliferative (in normal skin). The "Classical" senescence signature fails to identify nevus melanocytes (Mel 0 and Mel 1) as senescent, especially when compared with other cell types or other melanocytes. **C**. Extension of the analysis in panel B to eight additional signatures.

9

174   suppressing effects of noise (random positive and negative variation would tend to cancel out).

175   The results suggest that skin fibroblasts better fit the "Classical" senescent signature than any

176   skin cell type, including nevus melanocytes, or indeed melanocytes of any cluster. As a control—

177   to demonstrate the ability of this approach to correctly associate cell types with gene signatures—

178   we analyzed the same data using a signature of cell proliferation, "meta-PCNA", that represents

179   129 human genes most positively correlated with proliferation marker PCNA in a compendium of

180   normal tissues (Venet et al., 2011). As shown in Fig. 3B (also see Fig. S3), this signature (122

181   genes of which had unambiguous mouse orthologs; Data S1) identified two keratinocyte

182   populations ("IFE-cycling" and "Outer Bulge 1") as highly proliferative (in agreement with (Joost

183   et al., 2020)), and mature (postmitotic) keratinocytes as non-proliferative. Importantly, it also

184   correctly identified nevus melanocytes as non-proliferative—and other melanocytes as

185   proliferative—in agreement with Fig. 1E-F.

186   Figures 3C and S3 extend this analysis to the remaining eight potential signatures of

187   senescence (five consisting of genes that are upregulated; three of genes that are

188   downregulated). In five of the eight cases, nevus melanocytes rank as *less* senescent than the

189   average skin cell; in two of the cases nevus melanocytes are about average. In only one case

190   ("Chatsirisupachai Down") does nevus melanocyte gene expression go in the predicted direction

191   for senescence. However, the Chatsirisupachai signatures had not been curated to remove

192   genes associated simply with proliferation/quiescence (Chatsirisupachai et al., 2019), and

193   inspection of the "Chatsirisupachai Down" gene list shows that 61 of its 250 genes are shared

194   with the 129-gene meta-PCNA signature; i.e., it is more likely a signature of proliferation than

195   "non-senescence" (note the strong similarity between the "Chatsirisupachai Down" bar graph in

196   Fig. 3C and the meta-PCNA graph in Fig. 3B).

197   Together these data do not support the view that any sort of senescence—oncogene-induced

198   or otherwise—is characteristic of nevus melanocytes and therefore a possible cause of their

199   growth arrest.

Does a cell autonomous process arrest nevi?

200

201   As discussed above, OIS is usually presented as a cell-autonomous process [e.g. (Dankort et

202   al., 2009; Dhomen et al., 2009; Michaloglou et al., 2005; Serrano et al., 1997)]. The simplest cell-

203   autonomous process that one might imagine is a probabilistic switch: Once oncogene activation

204   commences, cells arrest with a fixed probability (per time or per cell cycle). Regardless of the

205   molecular details, such a model makes distinctive predictions about clonal dynamics.

206   Consider the clonal descendants of a single oncogene-transformed founder cell. For any

207   value of the per-cell-cycle senescence probability (which we denote here as "*s*"), how many cells

208   should we expect that clone to contain at any given time? How many cell cycles should it take

209   before all of the cells in most clones should have arrested? Such questions are well studied in

210   mathematics (Athreya & Ney, 1972), and easily solved by computer simulation. For this particular

211   problem, there are two key results (Figure 4).

212   First, the time after which one can expect clones to have stopped growing (e.g. when all cells

213   will have arrested in, say, 95% or 99% of clones) is a steep function of *s*. If *s* < 0.5, (i.e. less than

214   a 50% chance of arrest per cell cycle), then some clones will never stop growing. If *s* is, say,

215   0.53, all clones will eventually stop growing, but one must wait 51 cell cycles before 99% of them

216   do so (Fig. 4A). Given typical lengths of postnatal mammalian cell cycles, and the fact that we

217   observe cessation of mouse nevus growth in about 2-3 weeks, we may consider 30 to be a

218   generous estimate for the maximum number of cell cycles by which nevi stop growing. To achieve

219   99% clonal arrest by 30 cell cycles, *s* must be around 0.56 or higher; to achieve arrest in 95% of

220   clones, *s* must be greater than 0.52 (Fig. 4A).

221   From the same simulations one may also calculate predicted distributions of clone sizes.

222   There is a clear reciprocal relationship between mean clone size and the fraction of clones that

223   arrest by 30 cell cycles of time (Fig. 4B). For example, a value of *s* that enables 95% of clones

224   to arrest produces a mean clone size of only 18.5 cells. For comparison, we estimate cell

225   numbers per nevus to be in the range of 100-1000 cells (see Methods).

226   The explanation for the small mean clone sizes produced by simulations can be appreciated

227   by examining the full size distributions. As shown in Fig 4C-D, such distributions are extremely

228   heavy-tailed, with a very large number of very small clones and a small number of very large

229   clones (the histograms in Fig. 4C-D are plotted with logarithmic abscissa to facilitate display of all

230   clone sizes).

231   Qualitatively, this is very different from what we observed for nevi on the backs of p21 mice.

232   Nevi displayed a mean radius of 76.8 µm (corresponding to an area of 0.019 mm^2, in excellent

233   agreement with the results of (Damsky et al., 2015)) and. when plotted on a logarithmic scale,

234   individual radii displayed a Gaussian-like distribution (Fig. 4E; a Gaussian shape on a logarithmic

235   axis is usually referred to as "log-normal"). Interestingly, nest sizes (quantified by MPM) also

236   seem to be log-normally distributed whether at P21 (Fig. S4A) or P50 (Fig. S4B). So are the nests

237   within human melanocytic nevi, despite the latter being an order of magnitude larger than those

238   in mice (Fig. S4C). It should be noted that using different units to represent simulation results

239   (cell numbers) and empirical data (linear dimension) in Fig. 4 and S4 does not confound

11

240   comparing the shapes of distributions, thanks to the logarithmic abscissa: as long as cell number

241   scales as some power of linear dimension, values associated with log-transformed bins are simply
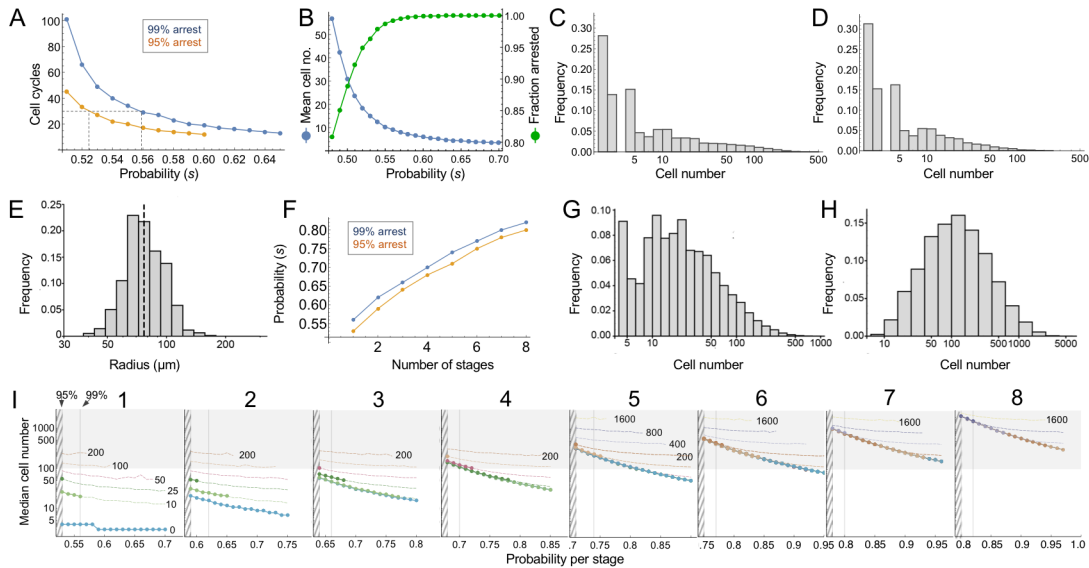
Figure 4. Modeling cell-autonomous clonal arrest as a probabilistic process. A-D. Monte Carlo simulations were carried out in which a single cell replicates and arrests with fixed probability, s, per cell cycle. **A.** Cell cycles required before proliferation stops in 95% or 99% of simulations. **B.** Mean cells at 30 cell cycles, and the fraction of clones that can be expected to have arrested by then. **C-D.** Clone (nevus) size distributions, after 30 cell cycles, assuming $s = 0.56$ (C) or 0.53 (D). **E.** Actual mouse nevus sizes at P21 (mice = 3, nevi = 768). Dashed line shows median radius, 76.8µm. **F-I.** Simulations in which proliferating cells arrest after multiple events (stages). **F.** The value of s required to ensure arrest within 30 cell cycles, as a function of number of stages. **G-H.** Clone size distributions for two (G), or three (H) stages, assuming the lowest per-stage transition probability compatible with 99% arrest by 30 cell cycles (see panel C). **I.** Median clone size for different numbers of stages (labeled above each graph), transition probabilities per stage (plotted on the abscissa), and thresholds below which clones are excluded from analysis. Each curve represents a different exclusion threshold (between 0 and 200 cells for 1-4 stages, and up to 1600 cells for 5-8 stages, as labeled). Curves become dashed at the point where the observability threshold exceeds 50% of the median cell number (values along the dashed segments require most observed nevi to be only barely larger than the limits of observation, which qualitatively disagrees with observations). Within the hatched region, fewer than 95% of clones arrest by 30 cell cycles. The thin line to right of the hatched region marks the probability at which 99% of clones arrest by 30 cell cycles. Solid gray demarcates median cell numbers between 100 and 3000 (see text). All results are from a minimum of 20,000 simulations.

242   scaled by a constant factor.

243   The above comparison of observed distributions with the results of computer simulation is not
244   entirely fair, however: Simulations track all clones, no matter how small, whereas empirical
245   distributions undoubtedly omit nevi with sizes below some threshold of observability. To correct
246   for this, one can truncate simulated distributions to remove clones smaller than some threshold
247   size. With no *a priori* way to know what threshold to use, we examined the entire range of
248   plausible truncations (up to the largest clone sizes). As it turns out, the relative shapes of
249   simulated distributions were about the same regardless of where they were truncated. The
250   reason for this behavior can be understood by displaying simulated distributions (with bin sizes of
251   one cell) on a log-log plot, and observing that they fall, over most clone size ranges, on a straight
252   line (see Supplemental Material). This implies an approximately "power law" relationship which,
253   by definition, is scale-free, i.e. has the same relative shape over any range of observations. In
254   fact, for *s* reasonably close to 0.5, the approximate probability of observing any clone size can be
255   shown analytically to vary inversely with the 3/2-power of size (for derivation, see Supplemental
256   Material).

257   These data imply that observed nevus size distributions cannot be generated by any cell-
258   autonomous, random, time independent, one-step process. But they do not speak to whether a
259   more complicated random process, for example, one with several steps, might suffice. To
260   address this, one can simulate clonal evolution under multi-step models. Again, dynamic
261   predictions can be made. First, to achieve clonal stopping times within 30 cell cycles, the
262   minimum per-step transition probability increases with the number of steps (Fig. 4F). For example,
263   if it takes three random events to arrest growth in 99% of clones, the average probability of each
264   event needs to be at least 0.66 per cell cycle; with five random events that number is 0.74.

265   Second, although distributions generated by such models still tend to be heavy-tailed (Fig.
266   4G), they become less so as the number of steps increases (Fig. 4H), gradually approaching
267   something that looks log-normal. This makes mathematical sense: as per-cell-cycle probabilities
268   approach unity, the system approaches a clock that simply ticks off a fixed number of cell cycles
269   before stopping. A scenario in which all clones stop at roughly the same time, plus or minus some
270   variation, necessarily produces a log-normal distribution, since the logarithm of cell size will be
271   proportional to the number of cell divisions.

272   To determine how many independent steps would be required for a random cell-autonomous
273   process to produce distributions that fit those we observed for nevi, we simulated up to eight
274   random stages, over a variety of transition probabilities (Fig. 4I). We subjected the results to a

13

275   range of possible truncations, from 0 to 1600 cells, to mimic any observability cutoffs in the

276   empirical data, and recorded the median clone sizes produced under each of these scenarios.

277   As described below (see Methods), we estimate that the average nevus has about 500-1000

278   cells, but given possible errors in the estimate, we consider here a range of values between 100

279   and 3000 (gray-shaded area in Fig. 4I). Subject to the constraint that enough clones must arrest

280   within 30 cell cycles, and that observation thresholds cannot be so high that the observed median

281   is less than twice the threshold, we find that, to produce nevi of even 200 cells requires 4-5

282   independent events (stages), depending on whether one requires 95% or 99% clonal arrest; to

283   reach 500 cells requires 6-7 events. To reach even larger numbers—as would be found in human

284   nevi, or in other mouse models (Chai et al., 2014)—would require even more stages.

Does a collective process arrest nevi?

286   The above results indicate that, to generate in vivo-like distributions of nevi, a process

287   something like a clock is needed, with cells either counting elapsed divisions (or time) since

288   oncogene activation, or progressing through a sufficiently large sequence of random processes,

289   with tightly controlled probabilities, so that the net outcome is clock-like.

290   Cell-autonomous counting of cell cycles (up to about 12) can occur in early, cleavage-stage

291   embryos (Tadros & Lipshitz, 2009), but no mechanism has been described to enable growing (as

292   opposed to merely cleaving) cells to track more than a small handful of divisions (or the equivalent

293   amount of time). Erosion of telomeres can mark the passage of large amounts of time in some

294   cells, but this does not seem to occur to any significant degree in nevus melanocytes (Michaloglou

295   et al., 2005)).

296   In contrast, if growth arrest is not cell-autonomous, but driven by cell-cell communication, then

297   clock-like behavior is easily achieved, without any sort of intrinsic cell memory: Consider a simple

298   communication circuit in which every cell's arrest probability is simply a monotonically increasing

299   function of the number of cells around it that have already arrested (Fig. 5A). This mechanism

300   describes a dynamically well-understood feedback process that normal tissues use to control size

301   (Lander, 2011; Lander et al., 2009). Termed "renewal control" (Buzi et al., 2015), because

302   differentiated cells control the probability that progenitor cells self-renew, the process is often

303   mediated by secreted TGF-β superfamily members such as myostatin. activin and GDF11

304   (Gokoffski et al., 2011; Lee et al., 2005). Because it implements the engineering principle of

305   "integral negative feedback", renewal control produces highly robust final population sizes that

306   are independent of parameters such as cell cycle speed or the starting numbers of cells (Buzi et
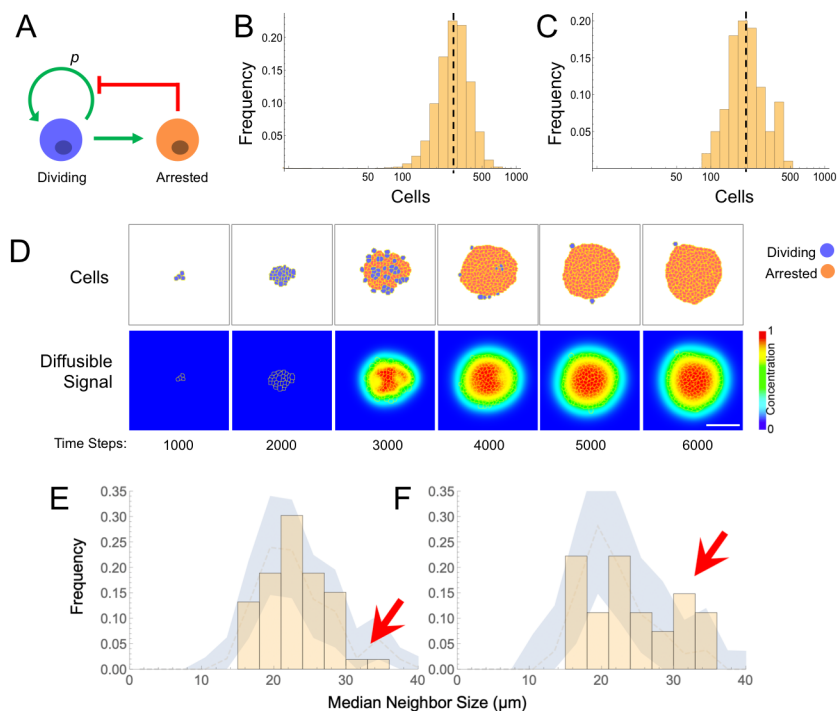
Figure 5. Models and evidence for cooperative, feedback-mediated arrest. A. A generic integral negative feedback scheme. "Renewal probability", *p*, is the probability that offspring of cell division remain dividing (i.e. 1-*p* is the probability that they arrest). **B.** Clone sizes generated by 9115 stochastic simulations of scheme A, modeled as an ordinary differential equation, where *p* falls with the number of arrested cells according to a Hill function with half-maximal effect at 50 arrested cells. **C-D.** Results from a spatial (agent-based) simulation of scheme A, in which the signal from arrested cells spreads by diffusion. Histogram (C) tabulates clone sizes produced by 100 independent simulations (the histograms in both B and C are logarithmically-scaled to show that the data are well fit by log-normal distributions). Panels (D) are from a single simulation, showing locations of growing and arresting cells, and the gradient of the diffusible signal. Bar = 50 μm. The average cell cycle is equivalent to approximately 382 Monte Carlo time steps. **E-F.** Using spatial coordinates and areas of 122 nests in seven individual fields at P21, nests were modeled as disks of equivalent area, and mean sizes of neighboring nests falling within successively larger annuli around each target nest were determined. Distributions of mean neighbor sizes up to 45 μm away from **(E)** large (radius >20μm) and **(F)** small (radius < 20μm) nests (histograms) are compared with a "null distribution" derived by random permutation (blue fields). Arrows show deviations in neighbor size distribution greater than expected at random, and substantially different for large versus small nests.

15

307   al., 2015; Lander, 2011; Lander et al., 2009).

308   When growth arrest due to renewal control is simulated as a probabilistic process (Fig. 5B),
309   the observed size distributions of clones is very close to log-normal. This is because renewal
310   control effectively enforces cell cooperation, so that once a small fraction of a clone has arrested,
311   the entire clone stops soon thereafter. The resulting narrow distribution of stopping times
312   produces size distributions that are approximately log-normal, i.e. that emulate a clock.

313   This behavior is a generic outcome of feedback control, and does not depend strongly on the
314   details of how feedback is implemented. Similar distributions are obtained whether we model
315   nevi as progressing reversibly or irreversibly through more than one proliferative stage, or use
316   agent-based simulations in which renewal is controlled by the concentration of a secreted
317   molecule that accumulates according to the laws of diffusion and local uptake (Fig. 5C-D). The
318   point of these simulations is not to argue in favor of a specific feedback mechanism, but rather to
319   show that, where cell-autonomous mechanisms of arrest struggle to fit nevus dynamics, almost
320   any sort of (collective) feedback does so easily.

321   Although nevus size distributions alone cannot shed light on the molecular details of how
322   feedback might be implemented in nevi, it is interesting that those cells that we identify as nevus
323   melanocytes (Fig. 2) express multiple genes encoding ligands with known or suspected growth
324   inhibitory activities, together with the receptors for those ligands. These include TGFβ superfamily
325   members *Gdf11*, *Gdf15*, *Tgfb1*, *Tgfb2*, and *Tgfb3*, as well as other genes associated with growth
326   inhibition, such as *Angptl2*, *Angptl4*, *Il6*, *Sema3a, Sema3b,* and *Sema3f* (Attisano & Wrana, 1996;
327   Neufeld et al., 2016; Santulli, 2014).

328   The evaluation of such candidates (as well as other genes expressed at too low a level to be
329   reliably detected by single cell RNA sequencing) will no doubt require further study. In the
330   meantime, we reasoned that any feedback mechanism based on secreted, diffusible factors
331   should induce spatial correlations among clones. In particular, when clones (or subclones) get
332   close enough to each other, they should inhibit each other's growth, leading to a smaller final size.
333   The distance over which such effects could occur should reflect the spatial decay length of
334   diffusible molecules in the skin, which is thought to be on the order of no more than a few hundred
335   microns (Chen et al., 2015). Although our data on macroscopic nevi (Fig. 1D), which had been
336   collected in a manner that included spatial coordinates, did not contain enough examples of nevus
337   spacings in this range to test this hypothesis, our data on the nests within individual nevi did, as
338   the median spacing between nests at postnatal day 21 was approximately 79 microns.

339 To assess whether nests were significantly smaller when located near other nests (especially
340 large ones), we extracted the coordinates and nest areas from 7 separate fields at P21
341 (representing 122 individual nests) and, modeling each nest as a disk of equivalent area,
342 calculated the mean sizes of neighboring nests falling within successively larger annuli around
343 each target nest. We compared the distributions of mean neighbor sizes near the 52 smallest
344 nests (radius <20 μm) with the equivalent distributions around the 70 largest nests.

345 As shown in Figure 5E-F, within annuli extending 45 μm away from the perimeters of target
346 nests, we saw fewer examples of large neighbors (radius > 30 μm) around large nests (panel E)
347 than around small ones (panel F). To determine whether the difference was statistically
348 significant, we used a permutation test in which we randomly swapped nest areas (but not
349 locations) within each field 5000 times, and recalculated the distributions. This allowed us to plot
350 the envelope enclosing the 5th and 95th percentiles for permuted data, onto which we overlaid the
351 observed data. Unlike the observed data, the envelopes of the permuted data (blue zones in Fig.
352 5E-F) look similar whether target nests are large or small. Moreover, the observed data extended
353 outside of the envelopes only for median neighbor sizes > 30 μm, with the data for small target
354 nevi extending well above the relevant envelope and the data for large target nevi lying at to the
355 bottom of the envelope (Fig. 5E-F, arrows). These results argue that proximity is associated with
356 a small, but significant decrease in nest size, supporting the view that nests inhibit each other's
357 growth. Interestingly, when we repeated the same analysis using annulus sizes of 150 μm,
358 differences in the sizes of neighbors of small and large nests were not seen, consistent with the
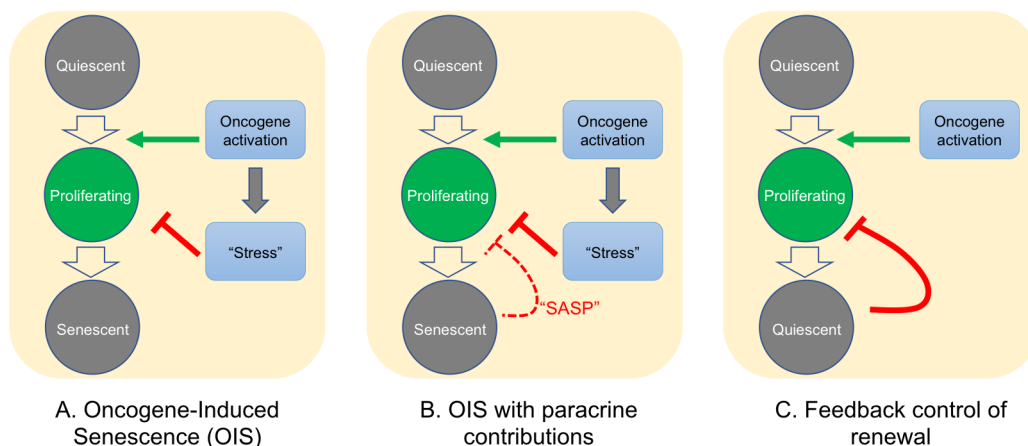359 view that whatever is promoting coordination among nests has a spatial range of <150 μm.

360 **DISCUSSION**

361 Studies in man, mouse and fish establish that most melanocytic nevi form by mutational activation
362 of BRAF, which triggers proliferation followed by growth arrest (Damsky & Bosenberg, 2017;
363 Dankort et al., 2009; Dhomen et al., 2009; Kaufman et al., 2016; Michaloglou et al., 2005; Patton
364 et al., 2005; Shain & Bastian, 2016). Nevus growth is often considered a paradigmatic example
365 of oncogene-induced senescence (OIS), but here we question two of the major tenets of the OIS
366 hypothesis: that nevus melanocytes are actually senescent; and that growth arrest is a direct
367 effect of oncogene action on the individual cell.

368 To assess whether nevi are senescent, we used single cell RNA sequencing in a mouse
369 model of *Braf*-driven nevus formation, comparing gene expression of nevus melanocytes with that
370 of other cell types. Across a wide variety of gene expression signatures, especially those
371 developed to distinguish senescence from other growth-arrested cell states, we failed to find any

372   evidence in support of the OIS hypothesis. By gene expression criteria, nevus melanocytes were

373   less senescent than many other normal skin cells, including non-nevus melanocytes (Fig. 3, S3).

374   These results support earlier work that also questioned, based on immunohistochemical staining

375   of human nevi for markers including lysosomal β-galactosidase, Ki67, p16^{INK4a} (*CDKN2A*), γ-H2AX

376   and p53, whether nevus melanocytes should be considered senescent (Tran et al., 2012). In

377   agreement with other studies, we do find that *Cdkn2A* is highly expressed in nevus cells; it is in

378   fact the only "classical" senescence marker that clearly distinguishes nevus melanocytes from

379   other melanocytes (Fig. 3A). Yet, as others have shown, *Cdkn2A* is neither necessary nor

380   sufficient for oncogene-mediated melanocyte growth arrest (Haferkamp et al., 2009; Zeng et al.,

381   2018). Thus, to the extent that nevus melanocytes do execute even part of a common senescence

382   program, there is little to support the view that this why they stop proliferating.

383   As for the question of exactly how *Braf*-induced nevus growth arrest occurs, Figure 6 presents

384   a continuum of models: In model A, oncogene action elicits a cell-autonomous stress response

385   which, after some time lag, triggers senescence that shuts proliferation down. This is the form in

386   which the OIS hypothesis is most frequently presented.

A. Oncogene-Induced Senescence (OIS)   B. OIS with paracrine contributions   C. Feedback control of renewal

Figure 6. Possible mechanisms of growth arrest. Three different models of nevus growth arrest are presented, varying from classical OIS (A) to feedback control of proliferative cell renewal (C). The model in the middle panel (B) illustrates a hypothetical hybrid situation, in which paracrine effects of senescence-associated secreted proteins (SASP) act as inhibitors of melanocyte self-renewal. Although model B can mimic some of the dynamic behaviors of model C, in the absence of convincing evidence that nevus melanocytes actually are senescent, we favor model C.

18

387   In model C, growth-arrest is not a direct effect of oncogene action, but rather a consequence
388   of growth itself. This type of feedback is commonly used by adult tissues to maintain constant
389   size, and also enables developing tissues to produce precise numbers of differentiated cells
390   (Kunche et al., 2016; Lander, 2011; Lander et al., 2009). Because of the collective nature of this
391   mechanism—cells that have stopped dividing tell other cells in their vicinity to do likewise—it
392   naturally produces semi-synchronous arrest of spatially-coherent cell clones, and the distinctive
393   log-normal clone size distribution that comes along with that. In contrast, a purely cell-
394   autonomous mechanism (panel A) has great difficulty producing such distributions (Fig. 4), either
395   necessitating the operation of some kind of multi-cell-cycle clock, or requiring cells to complete a
396   long sequence of independent probabilistic events prior to arresting (Fig. 4).

397   One can, of course, build a model in between these two extremes (model B), in which
398   oncogenes induce growth arrest directly, but paracrine signals (i.e. SASP factors) help maintain
399   it. If the paracrine role is important enough, this mechanism might also produce clone size
400   distributions that are approximately log-normal, so we cannot categorically rule this model out.
401   However, our gene expression data do not support any versions of it that have been explicitly
402   proposed for nevi. So far, several groups (working predominantly from in vitro observations) have
403   claimed a critical role for SASP factors in melanocyte OIS: Wajapeyee et al. (Wajapeyee et al.,
404   2008) argued that IGFBP7 plays a necessary role in the establishment of BRAF-V600E-induced
405   melanocyte senescence (a conclusion disputed by some (Scurr et al., 2010)); Feuerer et al.,
406   (Feuerer et al., 2019) proposed that MIA (melanoma inhibitory activity) secreted by senescent
407   melanocytes is required to maintain senescence; and Damsky and Bosenberg have proposed
408   that IL1, IL6, IL8 (encoded in mouse by *Cxcl15*), and type 1 interferons produced by nevus cells
409   play a role in their arrest (Damsky & Bosenberg, 2017).

410   Our in vivo data do not support any of these hypotheses. For example, we observed that the
411   vast majority of *Igfbp7* transcripts are produced by fibroblasts and endothelial cells and that,
412   among melanocytes, nevus melanocytes express lower levels of *Igfbp7* than non-nevus
413   melanocytes. We did not detect any *Mia* transcripts in nevus melanocytes, although it was
414   expressed at detectable levels in non-nevus melanocytes and various other skin cells. Likewise,
415   of *Il1* family members, only *Il1a* transcripts were detected in nevus melanocytes and they were at
416   levels lower than in many other skin cell types. *Il6* was also only weakly expressed in nevus
417   melanocytes, especially when compared with other cells. Transcripts for type 1 interferons were
418   not detected in any melanocytic cells, and *Cxcl15* transcripts were not detected in any skin cells
419   at all.

420   Of course, the accuracy of single cell RNA sequencing can be limited for weakly expressed

421   genes, so we cannot completely eliminate the possibility that these factors play some role in nevus

422   growth arrest.   But given these results, and the evidence that nevus melanocytes are not

423   senescent, we strongly favor the renewal-feedback model (model C). Adopting this model also

424   makes it easier to accommodate long-standing evidence that nevus growth arrest is not

425   permanent (Shain & Bastian, 2016). For example, it is known that nevi may exhibit a low level of

426   mitoses (Glatz et al., 2010); that they can grow in response to stimuli such as UV light (Rudolph

427   et al., 1998) or immunosuppression (Shain & Bastian, 2016) and, perhaps most tellingly, they can

428   re-grow after incomplete surgical resection—stopping again when they reach a typical nevus size

429   (Vilain et al., 2016). The latter result is inherently problematic for any non-feedback model, but is

430   precisely what renewal feedback predicts (Lander, 2011; Lander et al., 2009).

431   Because feedback control of renewal implements a generic strategy (integral negative

432   feedback (Lander, 2011)), it places no constraints on the molecular details of feedback, short of

433   the fact that whatever is mediating it needs to rise with the number of cells already arrested. One

434   possibility is that nevi are responding to some of the same signals that are used in melanocyte

435   homeostasis. For instance, during anagen phase of the hair cycle, melanocyte stem cells produce

436   progeny that migrate out of the hair follicle bulge as they differentiate, leaving functional stem

437   cells behind for future cycles. A variety of experimental and pathological circumstances that allow

438   small numbers of melanocytes to differentiate within the bulge cause differentiation and loss of

439   the entire stem cell pool (with concomitant hair graying (Nishimura et al., 2005)). This sort of

440   behavior—where differentiated cells drive the differentiation of their progenitors—is exactly the

441   sort of behavior that drives feedback models of renewal (Buzi et al., 2015; Lander, 2011; Lander

442   et al., 2009).

443   Nevi are but one of many types of benign, clonal, proliferative lesions that arise due to the

444   activation of oncogenes, but rarely if ever progress to malignancy (Adashek et al., 2020).

445   Notwithstanding the disruptive influence that oncogenes can have on cell physiology, the

446   existence of such lesions suggest that homeostatic mechanisms persist and function at many

447   stages along the road to cancer. New avenues for cancer prevention and treatment are likely to

448   follow from the detailed elucidation of such mechanisms.

449

450   **Experimental Design**

451   **Mouse treatment for nevus development**

452   *Braf*^{V600E}, *Tyr:Cre*ER (C56BL/6) mice were genotyped by PCR as previously described

453   (Bosenberg et al., 2006; Dankort et al., 2007). The primers used in this study are: Braf forward

20

454   5'-TGAGTATTTTTGTGGCAACTGC -3', Braf reverse 5'-CTCTGCTGGGAAAGCGCC -3', Cre

455   forward   5'-   GGTGTCCAATTTACTGACCGTACA-3'   and   Cre   reverse   5'-

456   CGGATCCGCCGCATAACCAGTG -3'. Topical administration of 4-hydroxytamoxifen (4-OHT;

457   25mg/mL or 75mg/mL in DMSO; 98% Z-isomer, Sigma-Aldrich) was administered to pups on their

458   back and/or paws at ages P2, P3, and P4. Images of nevi on back and paw skin were taken with

459   a digital camera at the indicated ages. Nevi from the underside of the skin were imaged using a

460   dissection microscope. All mouse procedures were approved by UCI's IACUC.

461

462   **Live imaging of the skin by multi-photon microscopy**

463   Mice were sedated, shaved, and depilated with wax strips at the indicated ages (during a

464   telogen phase) and the dorsal skin was imaged to capture the intrinsic fluorescent signal from

465   keratin, melanin, as well as the second-harmonic-generation signal from collagen, using the LSM

466   510 NLO Zeiss system. Excitation was achieved with a femtosecond Titanium: Sapphire

467   (Chameleon-Ultra, Coherent) laser at 900 nm. Emission was detected at 390-465 nm for second

468   harmonic generation (blue) and 500-550 nm (green) and 565-650 (red) for fluorescence.

469

470   *In vivo* **labeling with BrdU**

471   BrdU was prepared in sterile PBS at 10mg/mL and injected intraperitoneally into mice that

472   were 20 days old at 100mg/kg of body weight. 24 hours later the mouse was shaved, depilated

473   with wax strips and the skin was removed and fixed in 10% formalin for 16 hours.

474

475   **Immunofluorescence**

476   Formalin fixed paraffin embedded skins were sectioned 8μm thick, deparaffinized with Xylene,

477   and dehydrated in a series of increasing concentration of ethanol washes. Antigen retrieval was

478   performed with 10mM citric acid buffer at pH 6.0 for 10 min in a steamer. Samples were washed

479   with PBS, incubated with TrueBlack for 30 seconds to reduce autofluorescence, and washed

480   again with PBS. All antibodies were diluted at a 1:500 and incubated overnight at 4°C. Samples

481   were washed and incubated with the appropriate secondary antibody. Melanocytes were

482   identified with a Pmel antibody (EP4863(2); ab137078, Abcam). Cells that incorporated BrdU

483   were visualized with a BrdU antibody (ab6326, Abcam).

484

485   **Cell Isolation for Single Cell RNA Sequencing**

486   *Braf^WT^*, *Tyr*::*Cre*ER or *Braf^V600E^*, *Tyr*::*Cre*ER mice were euthanized at either P30 (n = 2 of each

487   genotype) or P50 (n = 3 of each genotype), shaved, and depilated. A 2x3 cm section of the dorsal

488   skin was removed, and the fat scraped off from the underside. The piece was then diced into

489   smaller pieces and suspended in dissociation buffer (RPMI, liberase 0.25mg/mL, Hepes 23.2 mM,

490   Sodium Pyruvate 2.32mM, Collagenase:Dispase 1mg/mL) for 50 minutes at 37°C with gentle

491   agitation. After incubation, DNaseI (232U) was added for 10 minutes and then inactivated with

492   fetal bovine serum and EDTA (1mM).   The tissue suspension was further dissociated

493   mechanically with the GentleMACS using the setting m_imptumor_04.01, which runs for 37

494   seconds at various speeds. Single cell suspensions were filtered twice through a 70µm strainer

495   and dead cells removed by centrifugation at 300 x g for 15 min. The live cells were washed with

496   0.04% UltraPure BSA:PBS buffer, gently re-suspended in the same buffer, and counted using

497   trypan blue.

498

499   **Library Preparation for Single Cell RNA Sequencing and Analysis**

500   Libraries were prepared using the Chromium Single Cell 3' v2 protocol (10X Genomics).

501   Briefly, individual cells and gel beads were encapsulated in oil droplets where cells were lysed

502   and mRNA was reverse transcribed to 10X barcoded cDNA. Adapters were ligated to the cDNA

503   followed by the addition of the sample index. Prepared libraries were sequenced using paired

504   end 100 cycles chemistry for the Illumina HiSeq 4000. FASTQ files were generated from

505   Illumina's binary base call raw output with Cell Ranger's (v2.1.0) `cellranger mkfastq` command

506   and the count matrix for each sample was produced with `cellranger count`. All ten samples (4

507   samples from P30 [two control (wild type) and two mutant] and 6 samples from P50 [three control

508   and three mutant]) were aggregated together with the `cellranger aggr` command to produce one

509   count matrix that includes all samples. Data analysis was performed with Scanpy [v1.3.6] (Wolf

510   et al., 2018). Cells with fewer than 200 detected genes, and genes detected in less than three

511   cells, were discarded. We calculated the percent mitochondrial gene expression and kept cells

512   with less than 13% mitochondrial gene expression, and cells with fewer than 4000 genes/cell

513   (35,141 cells). Each cell was normalized to total counts over all genes. In the final preprocessing

514   step, we regressed out cell-cell variation driven by mitochondrial gene expression and the number

515   of detected UMI. To identify clusters, we first performed principal component analysis on log-

516   transformed data, using highly variable genes, Louvain clustering (Levine et al., 2015), and

517   visualization with t-distributed stochastic neighbor embedding (tSNE).

518

519   **Quantification of nevus and nest size and cell content**

520   To quantify the sizes of nevi in mice, dorsal skin was excised and the underside visualized

521   using a dissecting microscope. Nevi were traced, and area calculated using ImageJ. Nest sizes

522   were quantified in live mice by MPM. Sizes of human nests were measured from histological

523   samples (n=5) obtained from the UCI Department of Dermatology. Samples were stained with

524   hematoxylin and eosin and imaged with a microscope. A dermatologist manually identified the

525   nests on each slide, and nest area was quantified using ImageJ. Human studies were performed

526   under IRB protocol HS# 2019-5054.

527   Estimates of cell numbers for mouse nevi were obtained in two different ways: First, we used

528   estimates from (Chai et al., 2014) for melanocytic nuclei per square area of mouse nevus, together

529   with our observed median nevus radius of 76.8 µm; this approach led to an estimate of 897

530   cells/nevus. As the data of (Chai et al., 2014) come from a different genetic model, we also

531   estimated cell number as follows: Using 8 µm sections of back skin from Albino Braf^{V600E} mice,

532   we used fluorescence microscopy to measure the sizes of 194 Pmel-stained melanocytes within

533   the nests of nevi, obtaining an average cell diameter of 5.68 µm, and counted approximately 14.4

534   cells per 10^4 µm^3 of nest. In pigmented animals, we measured by MPM an average nest cross

535   sectional area of 1385 µm^2, an average nest volume of 38792 µm^3, and an average number of

536   nests per nevi of approximately 12, yielding an estimate of 672 cells/nevus. Given uncertainties

537   in these measures, analyses in the manuscript take into account the possibility of an average that

538   falls anywhere between 100 and 1000 cells.

539

540   **Simulations and Agent-Based Modeling**

541   Stochastic, non-spatial simulations of renewal control were obtained by Monte Carlo

542   simulation, in which cells duplicated every cell cycle, and then chose randomly whether to

543   differentiate or continue dividing according to a probability modified by feedback from non-dividing

544   cells. A Hill function, with Hill coefficient =1, was used to represent the feedback.

545   To model feedback in a spatial context, we used CompuCell3D, an open-source platform for

546   Cellular Potts modeling (Swat et al., 2012). In CPM, every generalized object or "cell" is

547   associated with a list of attributes such as cell type, surface area, volume, etc. These enter into

548   the calculation of an effective energy, which can be summarized as the sum of the contact energy

549   between neighboring cells and the effective energy due to volume constraints.

550   Simulations were initialized by seeding a single cell, with a size of 25 pixel^2, in the center of a

551   300 X 300 pixel lattice, which grew and divided according to rules and parameters summarized

552   in Data S2. To add variability to cell growth, cells randomly chose one of three different growth

553   rates after every cell division. To add variability to cell division times, cells randomly chose a target

554   area, between 72 and 80 pixel^2, at which to divide. Growth rates were chosen to be sufficiently

555   slow that the mean time between cell divisions came out to approximately 382 time steps. At

556 division, each cell was divided in half by a randomly-oriented division plane.

557 Upon division, a cell either remained dividing or became permanently arrested. All cells had

558 a minimum 1% probability of arrest per cell division. Once an arrested cell was generated, it

559 began continuous secretion of a signaling molecule that diffuses and promotes the transition from

560 dividing to non-dividing (Kunche et al., 2016). Diffusion and decay of the feedback factor was

561 modeled deterministically, with parameters chosen to produce a steady state decay length of 15

562 pixels. The concentration of this factor at the center of mass of each cell then augmented the

563 arrest probability of that cell by an amount determined by a Hill function (see Data S2).

564

Statistical Analysis

566 Statistical analyses for single cell RNA sequencing were performed using Scanpy. Other

567 statistical testing was done using *Mathematica*. For the spatial analysis in Figure 5E-F, nest areas

568 in each field were randomly swapped, with positions held constant, 5000 times, and the

569 distributions of neighboring nest locations and sizes re-calculated each time. This allowed us to

570 generate an envelope enclosing the 5th and 95th percentiles for the permuted data, at each target

571 nest size, and compare the observed data with the bounds of that envelope.

572

References

574 Acosta, J. C., Banito, A., Wuestefeld, T., Georgilis, A., Janich, P., Morton, J. P., Athineos, D.,
575 Kang, T. W., Lasitschka, F., Andrulis, M., Pascual, G., Morris, K. J., Khan, S., Jin, H.,
576 Dharmalingam, G., Snijders, A. P., Carroll, T., Capper, D., Pritchard, C., Inman, G. J.,
577 Longerich, T., Sansom, O. J., Benitah, S. A., Zender, L., & Gil, J. (2013). A complex
578 secretory program orchestrated by the inflammasome controls paracrine senescence.
579 *Nat Cell Biol*, *15*(8), 978-990. https://doi.org/10.1038/ncb2784
580 Adashek, J. J., Kato, S., Lippman, S. M., & Kurzrock, R. (2020). The paradox of cancer genes in
581 non-malignant conditions: implications for precision medicine. *Genome Med*, *12*(1), 16.
582 https://doi.org/10.1186/s13073-020-0714-y
583 Athreya, K. B., & Ney, P. E. (1972). *Branching Processes* (2nd ed.). Dover.
584 Attisano, L., & Wrana, J. L. (1996). Signal transduction by members of the transforming growth
585 factor-beta superfamily. *Cytokine Growth Factor Rev*, *7*(4), 327-339.
586 https://doi.org/10.1016/s1359-6101(96)00042-1
587 Beausejour, C. M., Krtolica, A., Galimi, F., Narita, M., Lowe, S. W., Yaswen, P., & Campisi, J.
588 (2003). Reversal of human cellular senescence: roles of the p53 and p16 pathways.
589 *EMBO J*, *22*(16), 4212-4222. https://doi.org/10.1093/emboj/cdg417
590 Bennett, D. C. (2003). Human melanocyte senescence and melanoma susceptibility genes.
591 *Oncogene*, *22*(20), 3063-3069. https://doi.org/10.1038/sj.onc.1206446
592 Bosenberg, M., Muthusamy, V., Curley, D. P., Wang, Z., Hobbs, C., Nelson, B., Nogueira, C.,
593 Horner, J. W., 2nd, Depinho, R., & Chin, L. (2006). Characterization of melanocyte-
594 specific inducible Cre recombinase transgenic mice. *Genesis*, *44*(5), 262-267.
595 https://doi.org/10.1002/dvg.20205

596 Buzi, G., Lander, A. D., & Khammash, M. (2015). Cell lineage branching as a strategy for
597   proliferative control. *BMC Biol*, *13*, 13. https://doi.org/10.1186/s12915-015-0122-8
598 Campisi, J., & d'Adda di Fagagna, F. (2007). Cellular senescence: when bad things happen to
599   good cells. *Nat Rev Mol Cell Biol*, *8*(9), 729-740. https://doi.org/10.1038/nrm2233
600 Chai, E., Ferguson, B., Prow, T., Soyer, P., & Walker, G. (2014). Three-dimensional modelling
601   for estimation of nevus count and probability of nevus-melanoma progression in a
602   murine model. *Pigment Cell Melanoma Res*, *27*(2), 317-319.
603   https://doi.org/10.1111/pcmr.12195
604 Chatsirisupachai, K., Palmer, D., Ferreira, S., & de Magalhaes, J. P. (2019). A human tissue-
605   specific transcriptomic analysis reveals a complex relationship between aging, cancer,
606   and cellular senescence. *Aging Cell*, *18*(6), e13041. https://doi.org/10.1111/acel.13041
607 Chen, C. C., Wang, L., Plikus, M. V., Jiang, T. X., Murray, P. J., Ramos, R., Guerrero-Juarez, C.
608   F., Hughes, M. W., Lee, O. K., Shi, S., Widelitz, R. B., Lander, A. D., & Chuong, C. M.
609   (2015). Organ-level quorum sensing directs regeneration in hair stem cell populations.
610   *Cell*, *161*(2), 277-290. https://doi.org/10.1016/j.cell.2015.02.016
611 Collado, M., & Serrano, M. (2006). The power and the promise of oncogene-induced
612   senescence markers. *Nat Rev Cancer*, *6*(6), 472-476. https://doi.org/10.1038/nrc1884
613 Damsky, W. E., & Bosenberg, M. (2017). Melanocytic nevi and melanoma: unraveling a
614   complex relationship. *Oncogene*, *36*(42), 5771-5792.
615   https://doi.org/10.1038/onc.2017.189
616 Damsky, W. E., Micevic, G., Meeth, K., Muthusamy, V., Curley, D. P., Santhanakrishnan, M.,
617   Erdelyi, I., Platt, J. T., Huang, L., Theodosakis, N., Zaidi, M. R., Tighe, S., Davies, M. A.,
618   Dankort, D., McMahon, M., Merlino, G., Bardeesy, N., & Bosenberg, M. (2015).
619   mTORC1 activation blocks BrafV600E-induced growth arrest but is insufficient for
620   melanoma formation. *Cancer Cell*, *27*(1), 41-56.
621   https://doi.org/10.1016/j.ccell.2014.11.014
622 Dankort, D., Curley, D. P., Cartlidge, R. A., Nelson, B., Karnezis, A. N., Damsky, W. E., Jr., You,
623   M. J., DePinho, R. A., McMahon, M., & Bosenberg, M. (2009). Braf(V600E) cooperates
624   with Pten loss to induce metastatic melanoma. *Nat Genet*, *41*(5), 544-552.
625   https://doi.org/10.1038/ng.356
626 Dankort, D., Filenova, E., Collado, M., Serrano, M., Jones, K., & McMahon, M. (2007). A new
627   mouse model to explore the initiation, progression, and therapy of BRAFV600E-induced
628   lung tumors. *Genes Dev*, *21*(4), 379-384. https://doi.org/10.1101/gad.1516407
629 Davies, H., Bignell, G. R., Cox, C., Stephens, P., Edkins, S., Clegg, S., Teague, J., Woffendin,
630   H., Garnett, M. J., Bottomley, W., Davis, N., Dicks, E., Ewing, R., Floyd, Y., Gray, K.,
631   Hall, S., Hawes, R., Hughes, J., Kosmidou, V., Menzies, A., Mould, C., Parker, A.,
632   Stevens, C., Watt, S., Hooper, S., Wilson, R., Jayatilake, H., Gusterson, B. A., Cooper,
633   C., Shipley, J., Hargrave, D., Pritchard-Jones, K., Maitland, N., Chenevix-Trench, G.,
634   Riggins, G. J., Bigner, D. D., Palmieri, G., Cossu, A., Flanagan, A., Nicholson, A., Ho, J.
635   W., Leung, S. Y., Yuen, S. T., Weber, B. L., Seigler, H. F., Darrow, T. L., Paterson, H.,
636   Marais, R., Marshall, C. J., Wooster, R., Stratton, M. R., & Futreal, P. A. (2002).
637   Mutations of the BRAF gene in human cancer. *Nature*, *417*(6892), 949-954.
638   https://doi.org/10.1038/nature00766
639 Dhomen, N., Reis-Filho, J. S., da Rocha Dias, S., Hayward, R., Savage, K., Delmas, V., Larue,
640   L., Pritchard, C., & Marais, R. (2009). Oncogenic Braf induces melanocyte senescence
641   and melanoma in mice. *Cancer Cell*, *15*(4), 294-303.
642   https://doi.org/10.1016/j.ccr.2009.02.022
643 Elzi, D. J., Song, M., Hakala, K., Weintraub, S. T., & Shiio, Y. (2012). Wnt antagonist SFRP1
644   functions as a secreted mediator of senescence. *Mol Cell Biol*, *32*(21), 4388-4399.
645   https://doi.org/10.1128/MCB.06023-11

646 Feuerer, L., Lamm, S., Henz, I., Kappelmann-Fenzl, M., Haferkamp, S., Meierjohann, S.,
647   Hellerbrand, C., Kuphal, S., & Bosserhoff, A. K. (2019). Role of melanoma inhibitory
648   activity in melanocyte senescence. *Pigment Cell & Melanoma Research*, *32*(6), 777-791.
649   https://doi.org/10.1111/pcmr.12801
650 Glatz, K., Hartmann, C., Antic, M., & Kutzner, H. (2010). Frequent mitotic activity in banal
651   melanocytic nevi uncovered by immunohistochemical analysis. *Am J Dermatopathol*,
652   *32*(7), 643-649. https://doi.org/10.1097/DAD.0b013e3181d7ce6f
653 Gokoffski, K. K., Wu, H. H., Beites, C. L., Kim, J., Kim, E. J., Matzuk, M. M., Johnson, J. E.,
654   Lander, A. D., & Calof, A. L. (2011). Activin and GDF11 collaborate in feedback control
655   of neuroepithelial stem cell proliferation and fate. *Development*, *138*(19), 4131-4142.
656   https://doi.org/10.1242/dev.065870
657 Gorgoulis, V., Adams, P. D., Alimonti, A., Bennett, D. C., Bischof, O., Bishop, C., Campisi, J.,
658   Collado, M., Evangelou, K., Ferbeyre, G., Gil, J., Hara, E., Krizhanovsky, V., Jurk, D.,
659   Maier, A. B., Narita, M., Niedernhofer, L., Passos, J. F., Robbins, P. D., Schmitt, C. A.,
660   Sedivy, J., Vougas, K., von Zglinicki, T., Zhou, D., Serrano, M., & Demaria, M. (2019).
661   Cellular Senescence: Defining a Path Forward. *Cell*, *179*(4), 813-827.
662   https://doi.org/10.1016/j.cell.2019.10.005
663 Haferkamp, S., Scurr, L. L., Becker, T. M., Frausto, M., Kefford, R. F., & Rizos, H. (2009).
664   Oncogene-induced senescence does not require the p16(INK4a) or p14ARF melanoma
665   tumor suppressors. *J Invest Dermatol*, *129*(8), 1983-1991.
666   https://doi.org/10.1038/jid.2009.5
667 Hernandez-Segura, A., de Jong, T. V., Melov, S., Guryev, V., Campisi, J., & Demaria, M.
668   (2017). Unmasking Transcriptional Heterogeneity in Senescent Cells. *Curr Biol*, *27*(17),
669   2652-2660 e2654. https://doi.org/10.1016/j.cub.2017.07.033
670 Huang, J. M., Chikeka, I., & Hornyak, T. J. (2017). Melanocytic Nevi and the Genetic and
671   Epigenetic Control of Oncogene-Induced Senescence. *Dermatol Clin*, *35*(1), 85-93.
672   https://doi.org/10.1016/j.det.2016.08.001
673 Ito, Y., Hoare, M., & Narita, M. (2017). Spatial and Temporal Control of Senescence. *Trends
674   Cell Biol*, *27*(11), 820-832. https://doi.org/10.1016/j.tcb.2017.07.004
675 Joost, S., Annusver, K., Jacob, T., Sun, X., Dalessandri, T., Sivan, U., Sequeira, I., Sandberg,
676   R., & Kasper, M. (2020). The Molecular Anatomy of Mouse Skin during Hair Growth and
677   Rest. *Cell Stem Cell*, *26*(3), 441-457 e447. https://doi.org/10.1016/j.stem.2020.01.012
678 Joshi, S. S., Tandukar, B., Pan, L., Huang, J. M., Livak, F., Smith, B. J., Hodges, T., Mahurkar,
679   A. A., & Hornyak, T. J. (2019). CD34 defines melanocyte stem cell subpopulations with
680   distinct regenerative properties. *PLoS Genet*, *15*(4), e1008034.
681   https://doi.org/10.1371/journal.pgen.1008034
682 Kaplon, J., Homig-Holzel, C., Gao, L., Meissl, K., Verdegaal, E. M., van der Burg, S. H., van
683   Doorn, R., & Peeper, D. S. (2014). Near-genomewide RNAi screening for regulators of
684   BRAF(V600E) -induced senescence identifies RASEF, a gene epigenetically silenced in
685   melanoma. *Pigment Cell Melanoma Res*, *27*(4), 640-652.
686   https://doi.org/10.1111/pcmr.12248
687 Kaufman, C. K., Mosimann, C., Fan, Z. P., Yang, S., Thomas, A. J., Ablain, J., Tan, J. L.,
688   Fogley, R. D., van Rooijen, E., Hagedorn, E. J., Ciarlo, C., White, R. M., Matos, D. A.,
689   Puller, A. C., Santoriello, C., Liao, E. C., Young, R. A., & Zon, L. I. (2016). A zebrafish
690   melanoma model reveals emergence of neural crest identity during melanoma initiation.
691   *Science*, *351*(6272), aad2197. https://doi.org/351/6272/aad2197 [pii]
692 10.1126/science.aad2197
693 Kuilman, T., Michaloglou, C., Mooi, W. J., & Peeper, D. S. (2010). The essence of senescence.
694   *Genes Dev*, *24*(22), 2463-2479. https://doi.org/10.1101/gad.1971610
695 Kuilman, T., Michaloglou, C., Vredeveld, L. C., Douma, S., van Doorn, R., Desmet, C. J.,
696   Aarden, L. A., Mooi, W. J., & Peeper, D. S. (2008). Oncogene-induced senescence

697 relayed by an interleukin-dependent inflammatory network. *Cell*, *133*(6), 1019-1031.
698 https://doi.org/10.1016/j.cell.2008.03.039
699 Kunche, S., Yan, H., Calof, A. L., Lowengrub, J. S., & Lander, A. D. (2016). Feedback, Lineages
700 and Self-Organizing Morphogenesis. *PLoS Comput Biol*, *12*(3), e1004814.
701 https://doi.org/10.1371/journal.pcbi.1004814
702 Lander, A. D. (2011). Pattern, growth, and control. *Cell*, *144*(6), 955-969.
703 https://doi.org/10.1016/j.cell.2011.03.009
704 Lander, A. D., Gokoffski, K. K., Wan, F. Y., Nie, Q., & Calof, A. L. (2009). Cell lineages and the
705 logic of proliferative control. *PLoS Biol*, *7*(1), e15.
706 https://doi.org/10.1371/journal.pbio.1000015
707 Lee, S. J., Reed, L. A., Davies, M. V., Girgenrath, S., Goad, M. E., Tomkinson, K. N., Wright, J.
708 F., Barker, C., Ehrmantraut, G., Holmstrom, J., Trowell, B., Gertz, B., Jiang, M. S.,
709 Sebald, S. M., Matzuk, M., Li, E., Liang, L. F., Quattlebaum, E., Stotish, R. L., &
710 Wolfman, N. M. (2005). Regulation of muscle growth by multiple ligands signaling
711 through activin type II receptors. *Proc Natl Acad Sci U S A*, *102*(50), 18117-18122.
712 https://doi.org/10.1073/pnas.0505996102
713 Levine, J. H., Simonds, E. F., Bendall, S. C., Davis, K. L., Amir el, A. D., Tadmor, M. D., Litvin,
714 O., Fienberg, H. G., Jager, A., Zunder, E. R., Finck, R., Gedman, A. L., Radtke, I.,
715 Downing, J. R., Pe'er, D., & Nolan, G. P. (2015). Data-Driven Phenotypic Dissection of
716 AML Reveals Progenitor-like Cells that Correlate with Prognosis. *Cell*, *162*(1), 184-197.
717 https://doi.org/10.1016/j.cell.2015.05.047
718 Michaloglou, C., Vredeveld, L. C., Soengas, M. S., Denoyelle, C., Kuilman, T., van der Horst, C.
719 M., Majoor, D. M., Shay, J. W., Mooi, W. J., & Peeper, D. S. (2005). BRAFE600-
720 associated senescence-like cell cycle arrest of human naevi. *Nature*, *436*(7051), 720-
721 724. https://doi.org/10.1038/nature03890
722 Neufeld, G., Mumblat, Y., Smolkin, T., Toledano, S., Nir-Zvi, I., Ziv, K., & Kessler, O. (2016).
723 The role of the semaphorins in cancer. *Cell Adh Migr*, *10*(6), 652-674.
724 https://doi.org/10.1080/19336918.2016.1197478
725 Nishimura, E. K., Granter, S. R., & Fisher, D. E. (2005). Mechanisms of hair graying: incomplete
726 melanocyte stem cell maintenance in the niche. *Science*, *307*(5710), 720-724.
727 https://doi.org/10.1126/science.1099593
728 Patton, E. E., Widlund, H. R., Kutok, J. L., Kopani, K. R., Amatruda, J. F., Murphey, R. D.,
729 Berghmans, S., Mayhall, E. A., Traver, D., Fletcher, C. D., Aster, J. C., Granter, S. R.,
730 Look, A. T., Lee, C., Fisher, D. E., & Zon, L. I. (2005). BRAF mutations are sufficient to
731 promote nevi formation and cooperate with p53 in the genesis of melanoma. *Curr Biol*,
732 *15*(3), 249-254. https://doi.org/10.1016/j.cub.2005.01.031
733 Pollock, P. M., Harper, U. L., Hansen, K. S., Yudt, L. M., Stark, M., Robbins, C. M., Moses, T.
734 Y., Hostetter, G., Wagner, U., Kakareka, J., Salem, G., Pohida, T., Heenan, P., Duray,
735 P., Kallioniemi, O., Hayward, N. K., Trent, J. M., & Meltzer, P. S. (2003). High frequency
736 of BRAF mutations in nevi. *Nat Genet*, *33*(1), 19-20. https://doi.org/10.1038/ng1054
737 Rudolph, P., Tronnier, M., Menzel, R., Moller, M., & Parwaresch, R. (1998). Enhanced
738 expression of Ki-67, topoisomerase IIalpha, PCNA, p53 and p21WAF1/Cip1 reflecting
739 proliferation and repair activity in UV-irradiated melanocytic nevi. *Hum Pathol*, *29*(12),
740 1480-1487. https://doi.org/10.1016/s0046-8177(98)90019-3
741 Saager, R. B., Balu, M., Crosignani, V., Sharif, A., Durkin, A. J., Kelly, K. M., & Tromberg, B. J.
742 (2015). In vivo measurements of cutaneous melanin across spatial scales: using
743 multiphoton microscopy and spatial frequency domain spectroscopy. *J Biomed Opt*,
744 *20*(6), 066005. https://doi.org/10.1117/1.JBO.20.6.066005
745 Santulli, G. (2014). Angiopoietin-like proteins: a comprehensive look. *Front Endocrinol*
746 *(Lausanne)*, *5*, 4. https://doi.org/10.3389/fendo.2014.00004

747 Scurr, L. L., Pupo, G. M., Becker, T. M., Lai, K., Schrama, D., Haferkamp, S., Irvine, M.,
748   Scolyer, R. A., Mann, G. J., Becker, J. C., Kefford, R. F., & Rizos, H. (2010). IGFBP7 is
749   not required for B-RAF-induced melanocyte senescence. *Cell*, *141*(4), 717-727.
750   https://doi.org/10.1016/j.cell.2010.04.021
751 Serrano, M., Lin, A. W., McCurrach, M. E., Beach, D., & Lowe, S. W. (1997). Oncogenic ras
752   provokes premature cell senescence associated with accumulation of p53 and
753   p16INK4a. *Cell*, *88*(5), 593-602. http://www.ncbi.nlm.nih.gov/pubmed/9054499
754 Shain, A. H., & Bastian, B. C. (2016). From melanocytes to melanomas. *Nat Rev Cancer*, *16*(6),
755   345-358. https://doi.org/10.1038/nrc.2016.37
756 Swat, M. H., Thomas, G. L., Belmonte, J. M., Shirinifard, A., Hmeljak, D., & Glazier, J. A. (2012).
757   Multi-scale modeling of tissues using CompuCell3D. *Methods Cell Biol*, *110*, 325-366.
758   https://doi.org/10.1016/B978-0-12-388403-9.00013-8
759 Tadros, W., & Lipshitz, H. D. (2009). The maternal-to-zygotic transition: a play in two acts.
760   *Development*, *136*(18), 3033-3042. https://doi.org/10.1242/dev.033183
761 Tran, S. L., Haferkamp, S., Scurr, L. L., Gowrishankar, K., Becker, T. M., Desilva, C.,
762   Thompson, J. F., Scolyer, R. A., Kefford, R. F., & Rizos, H. (2012). Absence of
763   distinguishing senescence traits in human melanocytic nevi. *J Invest Dermatol*, *132*(9),
764   2226-2234. https://doi.org/10.1038/jid.2012.126
765 Venet, D., Dumont, J. E., & Detours, V. (2011). Most random gene expression signatures are
766   significantly associated with breast cancer outcome. *PLoS Comput Biol*, *7*(10),
767   e1002240. https://doi.org/10.1371/journal.pcbi.1002240
768 Vilain, R. E., McCarthy, S. W., & Scolyer, R. A. (2016). The regenerating naevus. *Pathology*,
769   *48*(2), 108-112. https://doi.org/10.1016/j.pathol.2015.12.009
770 Vredeveld, L. C., Possik, P. A., Smit, M. A., Meissl, K., Michaloglou, C., Horlings, H. M.,
771   Ajouaou, A., Kortman, P. C., Dankort, D., McMahon, M., Mooi, W. J., & Peeper, D. S.
772   (2012). Abrogation of BRAFV600E-induced senescence by PI3K pathway activation
773   contributes to melanomagenesis. *Genes Dev*, *26*(10), 1055-1069.
774   https://doi.org/10.1101/gad.187252.112
775 Wajapeyee, N., Serra, R. W., Zhu, X., Mahalingam, M., & Green, M. R. (2008). Oncogenic
776   BRAF induces senescence and apoptosis through pathways mediated by the secreted
777   protein IGFBP7. *Cell*, *132*(3), 363-374. https://doi.org/10.1016/j.cell.2007.12.032
778 Wiley, C. D., Flynn, J. M., Morrissey, C., Lebofsky, R., Shuga, J., Dong, X., Unger, M. A., Vijg,
779   J., Melov, S., & Campisi, J. (2017). Analysis of individual cells identifies cell-to-cell
780   variability following induction of cellular senescence. *Aging Cell*, *16*(5), 1043-1050.
781   https://doi.org/10.1111/acel.12632
782 Wolf, F. A., Angerer, P., & Theis, F. J. (2018). SCANPY: large-scale single-cell gene expression
783   data analysis. *Genome Biol*, *19*(1), 15. https://doi.org/10.1186/s13059-017-1382-0
784 Yu, Y., Schleich, K., Yue, B., Ji, S., Lohneis, P., Kemper, K., Silvis, M. R., Qutob, N., van
785   Rooijen, E., Werner-Klein, M., Li, L., Dhawan, D., Meierjohann, S., Reimann, M.,
786   Elkahloun, A., Treitschke, S., Dorken, B., Speck, C., Mallette, F. A., Zon, L. I., Holmen,
787   S. L., Peeper, D. S., Samuels, Y., Schmitt, C. A., & Lee, S. (2018). Targeting the
788   Senescence-Overriding Cooperative Activity of Structurally Unrelated H3K9
789   Demethylases in Melanoma. *Cancer Cell*, *33*(2), 322-336 e328.
790   https://doi.org/10.1016/j.ccell.2018.01.002
791 Zeng, H., Jorapur, A., Shain, A. H., Lang, U. E., Torres, R., Zhang, Y., McNeal, A. S., Botton, T.,
792   Lin, J., Donne, M., Bastian, I. N., Yu, R., North, J. P., Pincus, L., Ruben, B. S., Joseph,
793   N. M., Yeh, I., Bastian, B. C., & Judson, R. L. (2018). Bi-allelic Loss of CDKN2A Initiates
794   Melanoma Invasion via BRN2 Activation. *Cancer Cell*, *34*(1), 56-68 e59.
795   https://doi.org/10.1016/j.ccell.2018.05.014
796 Zhang, B., Ma, S., Rachmin, I., He, M., Baral, P., Choi, S., Goncalves, W. A., Shwartz, Y., Fast,
797   E. M., Su, Y., Zon, L. I., Regev, A., Buenrostro, J. D., Cunha, T. M., Chiu, I. M., Fisher,

798   D. E., & Hsu, Y. C. (2020). Hyperactivation of sympathetic nerves drives depletion of
799   melanocyte stem cells. *Nature*, *577*(7792), 676-681. https://doi.org/10.1038/s41586-020-
800   1935-3

801

815

816